

THREE-DIMENSIONAL HEAT, MOISTURE AND AIR TRANSFER IN UNSATURATED SOILS

H. R. THOMAS*, S. W. REES AND N. J. SLOPER

Queen's Buildings, PO Box 917, Cardiff, CF2 1XH, Wales

SUMMARY

A new three-dimensional numerical model of coupled heat, moisture and air transfer in unsaturated soil is presented. In particular, the model accommodates moisture transfer in the form of liquid and vapour flow and heat transfer arising from conduction, convection and latent heat of vaporization. The bulk flow of dry air and the movement of air in a dissolved state are also included. The theoretical basis of the model, the finite element solution of the spatial terms and finite difference solution of the temporal terms are briefly presented. Attention is focused on the verification of the new numerical solution. This is achieved via comparisons with independent solutions of heat, moisture and air transfer in an unsaturated soil. The physical problem considered includes the highly non-linear hydraulic properties of sand. Thermal conductivity is also included as a function of soil moisture content. Excellent correlation of results is shown thus providing confidence in the new model.

The new model is also applied to a number of test cases which illustrate the need for the development of a model which can fully include three-dimensional behaviour. In particular, three applications are presented each increasing in complexity. The first application illustrates three-dimensional heat transfer. This particular application is verified against existing commercial finite element software. Subsequent applications serve to illustrate how the coupled processes of heat moisture and air transfer combine to yield three-dimensional problems even within a simple geometric domain. Visualization of three-dimensional results is also addressed. © 1998 by John Wiley & Sons, Ltd.

Int. J. Numer. Anal. Meth. Geomech., Vol. 22, 75–95 (1998)

(No. of Figures: 7 No. of Tables: 2 No. of Refs: 21)

Key words: three-dimensional; heat; moisture; air; transfer; unsaturated; soil

1. INTRODUCTION

The demand for an improved understanding of the thermo-hydraulic behaviour of unsaturated soils arises from a number of sources, in particular, from recent developments within the fields of civil and environmental engineering. For example, some of the more recent applications include studies of the energy efficiency of buildings through analysis of the thermal performance of ground floor slabs, and analysis of moisture migration under thermal gradients set-up in new techniques for remediation of contaminated land. A further area of application concerns the disposal of high-level nuclear waste. This is a subject of major international importance and is viewed as a particularly significant research application of the current work.

*Correspondence to H. R. Thomas, Queen's Buildings, PO Box 917, Cardiff, CF2 1XH, Wales
Tel: +44 (01222) 874279 Fax: +44 (01222) 874597 E-mail: thomashr@cf.ac.uk

Considering further the disposal of nuclear waste. One method under consideration is that of deep geological burial, where the waste will be placed in a repository and a multibarrier containment concept will be employed to mitigate the transmission of radionuclides to the biosphere. Within the context of this concept the accurate prediction of the transfer of heat generated by the high level waste, the corresponding migration of moisture within the engineered barrier system and host material, and consequent changes in air pressure are viewed as important. Assessment of the overall performance of the system will depend on a clear understanding of these processes amongst others.¹

The design and performance assessment of barriers proposed to contain nuclear waste in underground repositories will ultimately require full-scale analyses which take into account discontinuities in the host material, which may result in zones of distinctly varying hydraulic properties, and more local heterogeneity caused by the drilling process. Detailed consideration of the significance of the geometrical configuration (possibly non-symmetric) will also be required. To this end, this paper presents the development of a three-dimensional model that is capable of describing fully coupled transfer of heat, moisture and air within the context of this type of practical engineering problem. The model is only applicable to non-deformable soil.

The theoretical formulation presented is based upon an approach developed by Thomas and Samsom.¹ Validation of the formulation has been considered previously in some detail. For example, a range of comparisons between numerical and experimental results has been provided by King.² The potential-based approach employed³ differs from the moisture content/temperature⁴ formulation more commonly adopted and the advantages of this are described elsewhere.⁵ Particular consideration has recently been given to validation of the air phase which is included in the current model.^{2,6,7} In view of the extensive work carried out previously, the basic theoretical formulation used here is taken to be of established validity.

The current work focuses on the development of a new three-dimensional model based on established theory and the necessary verification of the new computer software. The development of a numerical solution of the problem is briefly described. The finite element approach adopted was originally suggested by Zeinkiewicz and Taylor.⁸ Verification of the new model is achieved by a comparison of results with independent solutions.¹ This is followed by a number of applications of heat, moisture and air transfer through a small cubic domain and non-deformable sand. In particular, the applications serve to illustrate how three-dimensional behaviour can easily arise within the context of the coupled processes under consideration. The practical application of the new model gives rise to difficulties related to the need for visualisation of the three-dimensional numerical results. This problem is also addressed.

2. THEORY

The theoretical formulation employed considers flow through unsaturated soil as a three-phase system comprising solid particles, liquid and gas. The gas phase consists of a mixture of dry air and water vapour and the liquid phase is considered to be water which may contain dissolved air. The governing equations for moisture flow, as a combination of liquid transfer and vapour transfer, dry air flow and heat flow are briefly presented below. The governing equations are solved for the dependent variables capillary potential, temperature and air pressure. A more complete description of the theoretical formulation has been presented previously¹ and, therefore, only a brief summary of the formulation is included here.

2.1. The governing differential equation for moisture flow

A generalized form of Darcy's law is employed for non-isothermal liquid flow in an unsaturated soil. The unsaturated hydraulic conductivity is introduced as a function of moisture content and temperature by a relationship with the dynamic viscosity of water.⁹ The surface energy approach is used to express the capillary potential as a function of moisture content and temperature.¹⁰ Through the conservation of mass for liquid flow and employing the principle of partial derivatives the following equation for liquid flow is obtained:

$$C_{L\Psi} \frac{\partial \Psi}{\partial t} + C_{LT} \frac{\partial T}{\partial t} = \nabla[K_{L\Psi} \nabla \Psi] + \nabla[K_{La} \nabla P_a] + \nabla[K_{L\Psi} \nabla z] - \rho_1 E \quad (1)$$

where Ψ is the capillary potential, P_a is the air pressure and T is the temperature. ∇ is the vector differential operator which maintains full three dimensionality throughout the formulation. All terms are fully defined in the notation appendix.

The two effects of vapour pressure gradient and bulk flow of air are assumed to create vapour flow. These effects are related by using conservation of mass for vapour flow and assuming that liquid water is in equilibrium with water vapour.³ The effects of dry air velocity are introduced from Darcy's law for multiphase flow ignoring gravitational effects.¹¹ By taking into account the above effects and through appropriate substitution the following equation for vapour transfer is produced:

$$C_{V\Psi} \frac{\partial \Psi}{\partial t} + C_{VT} \frac{\partial T}{\partial t} = \nabla[K_{V\Psi} \nabla \Psi] + \nabla[K_{VT} \nabla T] + \nabla[K_{Va} \nabla P_a] + V_{V\Psi} \nabla \Psi + V_{VT} \nabla T + \rho_1 E \quad (2)$$

The governing equations for liquid (1) and vapour flow (2) are combined to yield the following equation for moisture flow

$$C_{\Psi\Psi} \frac{\partial \Psi}{\partial t} + C_{\Psi T} \frac{\partial T}{\partial t} = \nabla[K_{\Psi\Psi} \nabla \Psi] + \nabla[K_{\Psi T} \nabla T] + \nabla[K_{\Psi a} \nabla P_a] + V_{\Psi\Psi} \nabla \Psi + V_{\Psi T} \nabla T + \nabla[K_{L\Psi} \nabla z] \quad (3)$$

2.2. The governing differential equation for dry air flow

The isothermal transfer of dry air is assumed to be caused by two effects; the bulk flow of dry air and the transfer of dissolved air in liquid water.¹² The dissolved air is evaluated from Henry's coefficient of solubility¹³ and the flow of dry air by an application of the principle of conservation of mass. The dry air and water vapour are considered as ideal gases¹⁴ and Dalton's law of partial pressure is applied. The resulting equation is differentiated with respect to time and yields the governing differential equation for dry air flow as

$$C_{a\Psi} \frac{\partial \Psi}{\partial t} + C_{aT} \frac{\partial T}{\partial t} + C_{aa} \frac{\partial P_a}{\partial t} = \nabla[K_{a\Psi} \nabla \Psi] + \nabla[K_{aa} \nabla P_a] + V_{a\Psi} \nabla \Psi + V_{aT} \nabla T + V_{aa} \nabla P_a + \rho_{da} H_c \nabla \left[\frac{\partial K}{\partial z} \right] \quad (4)$$

2.3. The governing differential equation for heat flow

The effects of conduction, convection and latent heat of vaporization are included in the equation for heat flow. Convection results from the movement of liquid water, water vapour (from the vapour pressure gradient) and dry air. Latent heat is associated with the movement of water vapour from the vapour pressure gradient and as part of bulk flow of air. The principle of energy conservation is applied and the result is simplified to give the following governing differential equation for heat transfer:

$$C_{T\Psi} \frac{\partial \Psi}{\partial t} + C_{TT} \frac{\partial T}{\partial t} + C_{Ta} \frac{\partial P_a}{\partial t} = \nabla[K_{T\Psi} \nabla \Psi] + \nabla[K_{TT} \nabla T] + \nabla[K_{Ta} \nabla P_a] \\ + V_{T\Psi} \nabla \Psi + V_{TT} \nabla T + V_{Ta} \nabla P_a + C_{pl}(T - T_r) \nabla[K_{\Psi} \nabla z] \quad (5)$$

Together equations (3)–(5) define the complete theoretical formulation describing the coupled processes of moisture, air and heat flow in a three-dimensional unsaturated soil. These equations contain only three unknowns; the dependent variables Ψ (capillary potential), T (temperature) and P_a (pore air pressure).

3. THE NUMERICAL SOLUTION OF THE GOVERNING PARTIAL DIFFERENTIAL EQUATIONS

Due to the complexity of the theoretical formulation, numerical approximations are required to achieve the simultaneous solutions to the governing differential equations and the salient concepts of the numerical formulation employed have been described in detail elsewhere.^{8,15} A fully coupled spatial solution is achieved through the simultaneous solution of the three equations employing the finite element method, in particular, the Galerkin weighed-residual approach. The domain is discretised using three dimensional 20-node isoparametric ‘brick’ elements. Serendipity shape functions are used to approximate the unknown primary variables:

$$\begin{bmatrix} \Psi \\ T \\ P_a \end{bmatrix} \approx \begin{bmatrix} \hat{\Psi} \\ \hat{T} \\ \hat{P}_a \end{bmatrix} = \sum_{s=1}^{20} N_s \begin{bmatrix} \Psi_s \\ T_s \\ P_{as} \end{bmatrix} \quad (6)$$

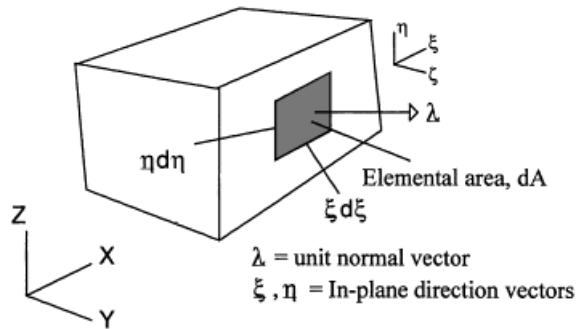


Figure 1. Boundary flux on a 20 noded isoparametric ‘brick’ element

where $\hat{\Psi}$, \hat{T} and \hat{P}_a are the approximate values of capillary potential, temperature and pore air pressure, respectively, and N_s are the standard serendipity shape functions.⁸

After application of the Gauss-Green divergence theorem, which introduces surface integrals that accommodate the summation of fluxes normal to the boundary surface and by substitution of the derivatives of the shape function approximations given in equations (6) the three governing equations (3)–(5) may be recast as shown below:

The spatial discretization of the governing equation for moisture transfer yields:

$$\begin{aligned} & \int_{\Omega^e} [K_{\Psi\Psi} \nabla \mathbf{N}_r \nabla \mathbf{N}_s] d\Omega^e \Psi_s + \int_{\Omega^e} [K_{\Psi T} \nabla \mathbf{N}_r \nabla \mathbf{N}_s] d\Omega^e \mathbf{T}_s + \int_{\Omega^e} [K_{\Psi a} \nabla \mathbf{N}_r \nabla \mathbf{N}_s] d\Omega^e \mathbf{P}_{as} \\ & - \int_{\Omega^e} [\mathbf{N}_r V_{\Psi\Psi} \nabla \mathbf{N}_s] d\Omega^e \Psi_s - \int_{\Omega^e} [\mathbf{N}_r V_{\Psi T} \nabla \mathbf{N}_s] d\Omega^e \mathbf{T}_s + \int_{\Omega^e} [\mathbf{N}_r C_{\Psi\Psi} \mathbf{N}_s] d\Omega^e \frac{\partial \Psi_s}{\partial t} \\ & + \int_{\Omega^e} [\mathbf{N}_r C_{\Psi T} \mathbf{N}_s] d\Omega^e \frac{\partial \mathbf{T}_s}{\partial t} + \int_{\Omega^e} [K_{la} \nabla \mathbf{N}_r \nabla z] d\Omega^e - \int_{\Gamma^e} \mathbf{N}_r \rho_1 [\mathbf{v}_{ln} + \mathbf{v}_{vn}] d\Gamma^e = 0 \end{aligned} \quad (7)$$

The spatial discretization of the governing equation for heat transfer yields:

$$\begin{aligned} & \int_{\Omega^e} [K_{TT\Psi} \nabla \mathbf{N}_r \nabla \mathbf{N}_s] d\Omega^e \Psi_s + \int_{\Omega^e} [K_{TTT} \nabla \mathbf{N}_r \nabla \mathbf{N}_s] d\Omega^e \mathbf{T}_s + \int_{\Omega^e} [K_{Ta} \nabla \mathbf{N}_r \nabla \mathbf{N}_s] d\Omega^e \mathbf{P}_{as} \\ & - \int_{\Omega^e} [\mathbf{N}_r V_{TT\Psi} \nabla \mathbf{N}_s] d\Omega^e \Psi_s - \int_{\Omega^e} [\mathbf{N}_r V_{TTT} \nabla \mathbf{N}_s] d\Omega^e \mathbf{T}_s - \int_{\Omega^e} [\mathbf{N}_r V_{Ta} \nabla \mathbf{N}_s] d\Omega^e \mathbf{P}_{as} \\ & + \int_{\Omega^e} [\mathbf{N}_r C_{TT\Psi} \mathbf{N}_s] d\Omega^e \frac{\partial \Psi_s}{\partial t} + \int_{\Omega^e} [\mathbf{N}_r C_{TTT} \mathbf{N}_s] d\Omega^e \frac{\partial \mathbf{T}_s}{\partial t} + \int_{\Omega^e} [\mathbf{N}_r C_{Ta} \mathbf{N}_s] d\Omega^e \frac{\partial \mathbf{P}_{as}}{\partial t} \\ & + \int_{\Omega^e} [C_{pl}(T - T) K_{l\Psi} \nabla \mathbf{N}_r \nabla z] d\Omega^e - \int_{\Gamma^e} \mathbf{N}_r [\mathbf{F}_{lh1} + \mathbf{F}_{h2} + \mathbf{F}_{h3} + \mathbf{F}_{h4} + \mathbf{F}_{h5}] d\Gamma^e = 0 \end{aligned} \quad (8)$$

The spatial discretization of the governing equation for dry air transfer yields:

$$\begin{aligned} & \int_{\Omega^e} [K_{a\Psi} \nabla \mathbf{N}_r \nabla \mathbf{N}_s] d\Omega^e \Psi_s + \int_{\Omega^e} [K_{as} \nabla \mathbf{N}_r \nabla \mathbf{N}_s] d\Omega^e \mathbf{P}_{as} - \int_{\Omega^e} [\mathbf{N}_r V_{a\Psi} \nabla \mathbf{N}_s] d\Omega^e \Psi_s \\ & - \int_{\Omega^e} [\mathbf{N}_r V_{aT} \nabla \mathbf{N}_s] d\Omega^e \mathbf{T}_s - \int_{\Omega^e} [\mathbf{N}_r V_{aa} \nabla \mathbf{N}_s] d\Omega^e \mathbf{P}_{as} + \int_{\Omega^e} [\mathbf{N}_r C_{a\Psi} \mathbf{N}_s] d\Omega^e \frac{\partial \Psi_s}{\partial t} \\ & + \int_{\Omega^e} [\mathbf{N}_r C_{aT} \mathbf{N}_s] d\Omega^e \frac{\partial \mathbf{T}_s}{\partial t} + \int_{\Omega^e} [\mathbf{N}_r C_{aa} \mathbf{N}_s] d\Omega^e \frac{\partial \mathbf{P}_{as}}{\partial t} + \int_{\Omega^e} [\rho_{da} H_c K_{l\Psi} \nabla \mathbf{N}_r \nabla z] d\Omega^e \\ & - \int_{\Gamma^e} \mathbf{N}_r \rho_{da} [\mathbf{v}_{fn} + \mathbf{v}_{dn}] d\Gamma^e = 0 \end{aligned} \quad (9)$$

Equations (7)–(9) may be combined and written more conveniently in matrix notation as

$$\begin{bmatrix} \mathbf{K}_{\Psi\Psi} & \mathbf{K}_{\Psi T} & \mathbf{K}_{\Psi a} \\ \mathbf{K}_{T\Psi} & \mathbf{K}_{TT} & \mathbf{K}_{Ta} \\ \mathbf{K}_{a\Psi} & \mathbf{K}_{aT} & \mathbf{K}_{aa} \end{bmatrix} \begin{Bmatrix} \Psi_s \\ \mathbf{T}_s \\ \mathbf{P}_{as} \end{Bmatrix} + \begin{bmatrix} \mathbf{C}_{\Psi\Psi} & \mathbf{C}_{\Psi T} & - \\ \mathbf{C}_{T\Psi} & \mathbf{C}_{TT} & \mathbf{C}_{Ta} \\ \mathbf{C}_{a\Psi} & \mathbf{C}_{aT} & \mathbf{C}_{aa} \end{bmatrix} \begin{Bmatrix} \dot{\Psi}_s \\ \dot{\mathbf{T}}_s \\ \dot{\mathbf{P}}_{as} \end{Bmatrix} + \begin{Bmatrix} \mathbf{J}_{\Psi} \\ \mathbf{J}_T \\ \mathbf{J}_s \end{Bmatrix} = \{0\} \quad (10)$$

The vector \mathbf{J} is composed of gravity and flux boundary terms. Equation (10) may be rewritten as

$$\mathbf{K}\Phi + \mathbf{C} \frac{\partial \Phi}{\partial t} + \mathbf{J} = 0 \quad (11)$$

The boundary fluxes are evaluated as a normal flow acting on an element face using a method similar to that suggested by Irons and Ahmad.¹⁶ This method has been adapted from the structural terms of force and load¹⁶ to represent the appropriate flux terms encountered within the heat, moisture and air transfer model.

The elemental area dA is evaluated by finding the magnitude of the cross product of the two in-plane direction vectors:

$$dA = |\xi \times \eta| d\xi d\eta \quad (12)$$

Where η and ξ are local co-ordinates. The nodal components are then given by

$$\lambda_i = \int_{-1}^{+1} \int_{-1}^{+1} N_i \lambda \hat{\lambda}_i |\xi \times \eta| d\xi d\eta \quad (13)$$

where the subscript i refers to the nodal value, $\hat{\cdot}$ refers to the approximate value and λ is the flux component which is assumed to be always acting normal to the surface. The unit vector $\hat{\lambda}$, therefore, is given by

$$\hat{\lambda} = \frac{\xi \times \eta}{|\xi \times \eta|} \quad (14)$$

and therefore the nodal components are given by

$$\lambda_i = \int_{-1}^{+1} \int_{-1}^{+1} \mathbf{N}_i \lambda \xi \times \eta d\xi d\eta \quad (15)$$

To obtain the temporal solution to equation (11) a fully implicit mid-interval backward difference algorithm is employed. For a mid-interval backward difference scheme equation (11) may be rearranged and simplified to give

$$\Phi^{n+1} = \left[\mathbf{K}^{n+1/2} + \frac{\mathbf{C}^{n+1/2}}{\Delta t} \right]^{-1} \cdot \left[\frac{\mathbf{C}^{n+1/2} \Phi^n}{\Delta t} - \mathbf{J}^{n+1/2} \right] \quad (16)$$

A solution for Φ^{n+1} is obtained by calculating the coefficients \mathbf{K} , \mathbf{C} and \mathbf{J} at the mid-time interval $n + 1/2$. This is achieved using a predictor–corrector iterative solution procedure. A converged solution is assumed to have been achieved when the difference between successive iterations falls below a specified tolerance.

4. MODEL VERIFICATION

The validity of the theoretical formulation previously adopted for a two-dimensional model for heat, moisture and air transfer¹ has been shown through comparison of numerical results with experimental results.^{2,6,7} Therefore, verification of the new three-dimensional formulation was considered through a comparison of numerical results with a two-dimensional flow analysis of fully coupled heat, moisture and air transfer in unsaturated soil.¹ Full validation of the three-dimensional model against experimental data is not possible at the current time due to a lack of appropriate experimental data.

The analysis used for verification of the three-dimensional model illustrates the effects of thermal drying, as a result of elevated temperatures, hydration, due to recovery of ground water level, and the influence of elevated air pressures. The original two-dimensional analysis considered a 100 mm column of sand comprised of fifty uniform isoparametric eight noded elements with dimensions 2 mm \times 20 mm as shown in Figure 2(a). The new three-dimensional model was used to re-analyse this problem. A three-dimensional mesh was developed adopting similar discretization using fifty, 20-node isoparametric elements, of dimensions 2 mm \times 20 mm \times 20 mm, as shown in Figure 2(b). The material employed is unsaturated natural Leighton Buzzard medium sand with material parameters independently measured.^{17,18} The material properties required in the numerical model are defined in Table I.

A uniform set of initial conditions are employed throughout the domain; a capillary potential of -0.5 m, representing an initial moisture content of 1.7 per cent, air pressure is set at an atmosphere value of 100 kPa and the initial temperature is 293 K. Dirichlet boundary conditions were applied to the top and bottom faces of the column. The lower face of the column was subject to an elevated temperature of 50°C to represent heat generated by a waste source. The upper surface was prescribed at a capillary potential of -0.3 m simulating infiltration. Air pressure at the upper surface is at an initial value of 100 kPa and is allowed to increase to a prescribed threshold value of 102 kPa. This enables the air pressure to increase in the sample to this threshold value at such time it is allowed to escape. At this time the capillary potential is decreased to the initial value of -0.5 m. An initial timestep size of 10 s is employed which is allowed to increase to a maximum size of 900 s. This increase in timestep size is controlled by a factor which is a function of the number of iterations required to provide a converged solution.

Results are shown in Figures 3(a) and 3(b). Figure 3(a) shows temperature distribution at various times taken at sampling points spaced at 4 mm intervals. The sampling points have been taken from the midsides of each element face and have proved to be identical at corresponding depths to those achieved by Thomas and Sansom.¹ As would be expected the temperature

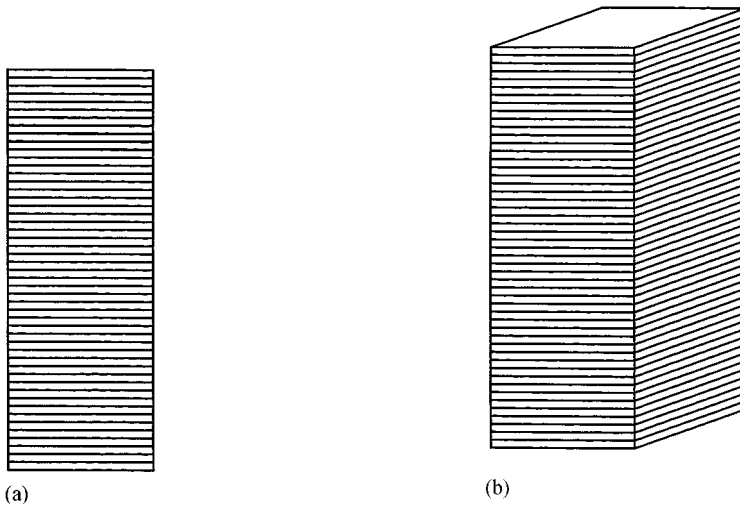


Figure 2. Verification—Column finite element meshes: (a) 2D; (b) 3D

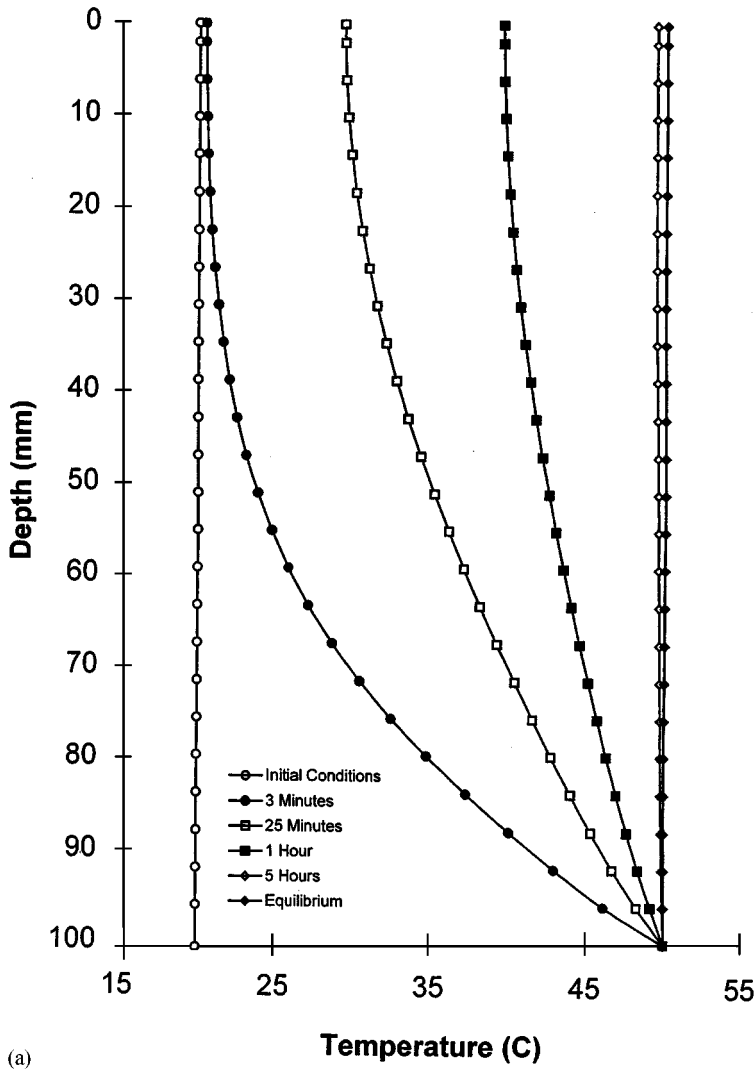


Figure 3. Verification—Transient variations with depth: (a) Temperature; (b) Capillary potential

throughout the domain steadily increases due to the effect of the elevated temperature boundary until a steady-state condition is achieved at a time in excess of 5 h. Figure 3(b) shows capillary potential distributions shown at various times taken at the same sampling points as mentioned in the previous Figure 3(a). Again results from Thomas and Sansom¹ were found to be identical at corresponding depths. A full description of the behaviour exhibited by the capillary potential profiles is provided by Thomas and Sansom¹ and for conciseness is not repeated here.

It is encouraging to note the high degree of agreement between the new three-dimensional model and an independent two-dimensional model. This analysis is one of many similar exercises

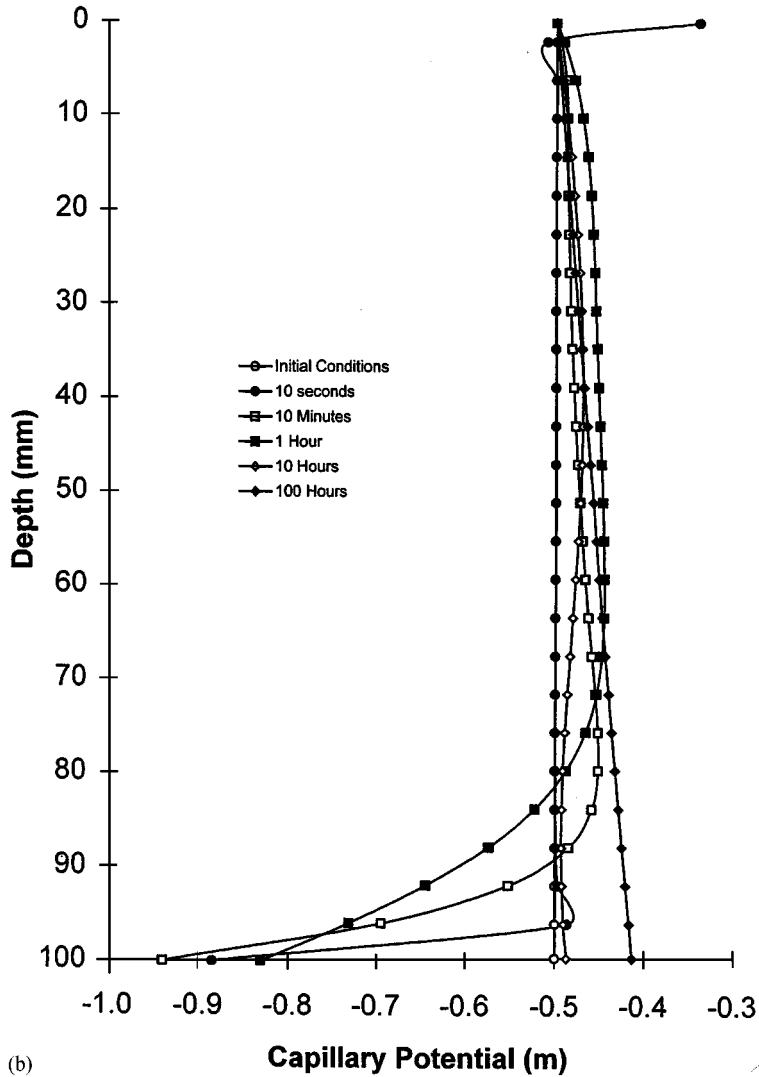


Figure 3 (Continued)

that have been carried out in order to verify the new model. In total a series of some 18 verification exercises have been completed yielding a high degree of confidence in the three-dimensional model.

5. THREE-DIMENSIONAL APPLICATIONS

Following verification of the new model a number of applications have been considered to investigate the three-dimensional behaviour of heat, moisture and air flow through unsaturated

soil. Some of the applications undertaken in this respect are presented below. All applications use the same material, Leighton Buzzard medium sand (described above), and the same spatial domain.

5.1. Finite element discretisation

The domain is shown in Figure 4(a) and consists of 64 regular cubic elements of dimension $12.5 \times 12.5 \times 12.5$ mm resulting in an overall cubic domain of dimension $50 \times 50 \times 50$ mm. The domain has been restricted to this size in the first instance due to the high computational (CPU) time taken to obtain a solution.

Using a three-dimensional domain can lead to difficulty for the reader regarding the interpretation of results and as a result this paper will endeavour to provide a consistent nomenclature. Figures 4(b) and 4(c) show definitions for plane cross-sections, cube faces, one-dimensional cross sections and the co-ordinate system. The vertical dimension is labelled Z for a consistent nomenclature with elevation (z) and therefore co-ordinates are given in the order X, Y, Z throughout. A plane across the Y and Z dimensions at a distance of $X = 0$ mm will be known as $X0$.

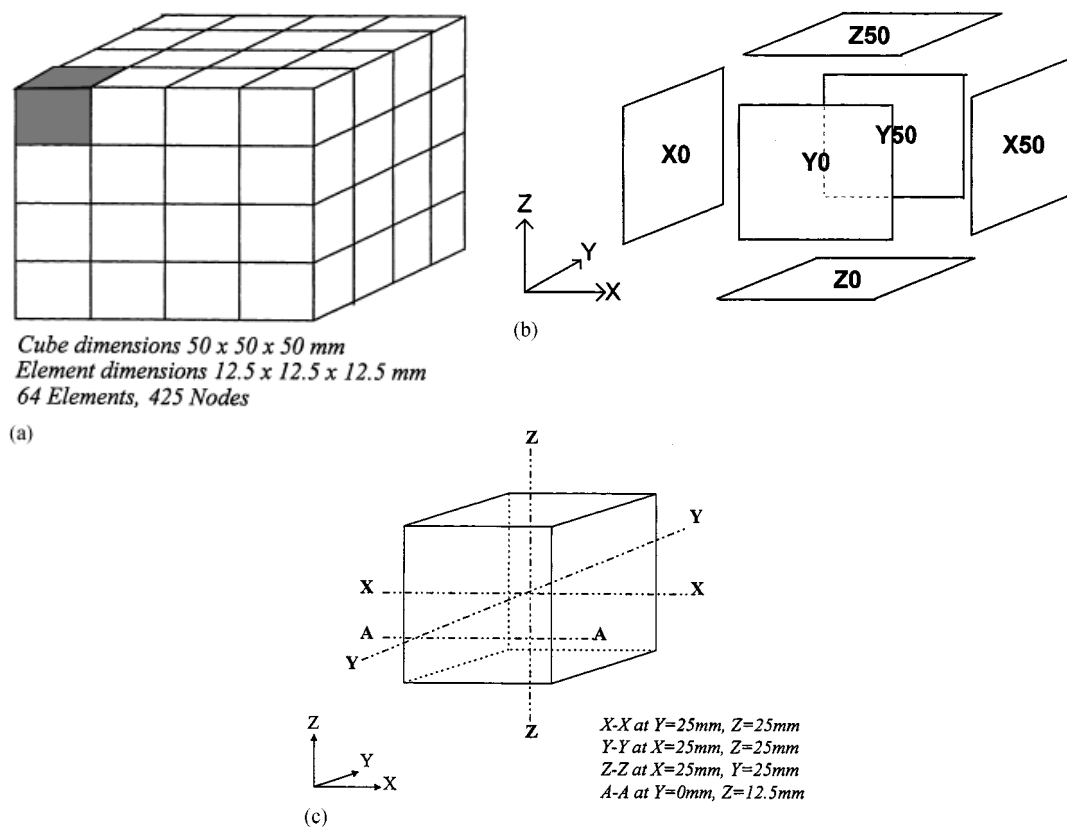


Figure 4. Cube domain: (a) Finite element mesh; (b) Faces; (c) 1D cross sections

Similarly a plane in the X and Y dimensions at a vertical height of $Z = 50$ mm (i.e., the top surface of the domain) will be known as $Z50$. One-dimensional cross-sections are taken at the centre of a cube face through the domain as shown in Figure 4(c). For instance $X-X$ provides a spatial variation in the X dimension through the centre of the YZ plane (i.e., $Y = Z = 25$ mm).

An additional factor that can require clarification arrives from the use of capillary potential (Ψ) as the primary variable describing unsaturated moisture transfer. The units of this variable are that of negative head ($-\Psi$ m), therefore, the larger the absolute value of capillary potential the lower the soil moisture content.

5.2. Application 1—Thermal application

The first application only considers heat conduction and the problem is run uncoupled with values of capillary potential (Ψ) and air pressure (P_a) held constant at values of -0.5 m and 100 kPa (≈ 1 atm), respectively. Initial temperatures throughout the domain are set uniformly at a value of 20°C . Dirichlet boundary conditions are set at all the faces of the domain and provide thermal gradients in the three dimensions. Faces $X0$, $Y0$ and $Z0$ are set at an elevated temperature of 60°C with faces $X50$, $Y50$ and $Z50$ held at the initial temperature of 20°C . For temporal changes a variable time-stepping procedure is adopted. An initial timestep size of 10 s is employed which is allowed to increase, subject to certain convergence criteria, to a maximum value of 50 s.

Results are presented in Figures 5(a) to 5(c). Figures 5(a) and 5(b) show contours of temperature taken at times of 10 s and 600 s, respectively, through plane section $Y12.5$ (i.e. a ZX plane at a distance of $Y = 12.5$ mm). Figure 5(a) shows temperatures are highest adjacent to the prescribed boundary on faces $X0$ and $Z0$. Figure 5(b) shows the same plane ($Y12.5$) taken at the equilibrium position of 600 s. It may be seen that the overall domain has, as would be expected, increased in temperature. It can also be seen that the mid-temperature, the average of the two boundary conditions at 40°C , is offset from the centre of the $X0$ - $X50$ and $Z0$ - $Z50$ gradients. This can be attributed to the $Y0$ - $Y50$ gradient in the Y direction increasing the overall temperature at the cross-section position. Figure 5(c) shows plane sections $Y25$ and $Z25$ at the equilibrium time of 600 s. The Figure shows temperature distribution through the domain with red representing a temperature of 60°C and blue a temperature of 20°C . This figure qualitatively shows the thermal distribution through the cube is clearly three dimensional.

A further verification exercise was conducted using a commercial finite element software package for three dimensional heat flow.¹⁹ The identical spatial domain used in Application 1 was modelled using PAFEC. The PAFEC software only considered heat conduction and therefore the material properties required for this software were those of specific heat capacity and thermal conductivity. The value adopted for specific heat capacity was 800 J/kgK (Table I) and the value for thermal conductivity of 1.7126 W/mK. The constant value for thermal conductivity was achieved by substituting the constant initial capillary potential value of -0.5 m into the $\psi v \theta$ relation (Table I) yielding a volumetric liquid content of 1.7 per cent and substituting this value into the $\lambda_c v \theta_1$ relation (also given in Table I).

Results for this analysis are shown in Figure 5(d). The figure makes a comparison of temperature profiles, across section $X-X$ (see Figure 4(c)), obtained by the new three-dimensional model and by the PAFEC model at equilibrium. This figure clearly demonstrates the high level of quantitative agreement between the thermal response of the new and alternative models and confidence in the validity of the new model has been further enhanced.

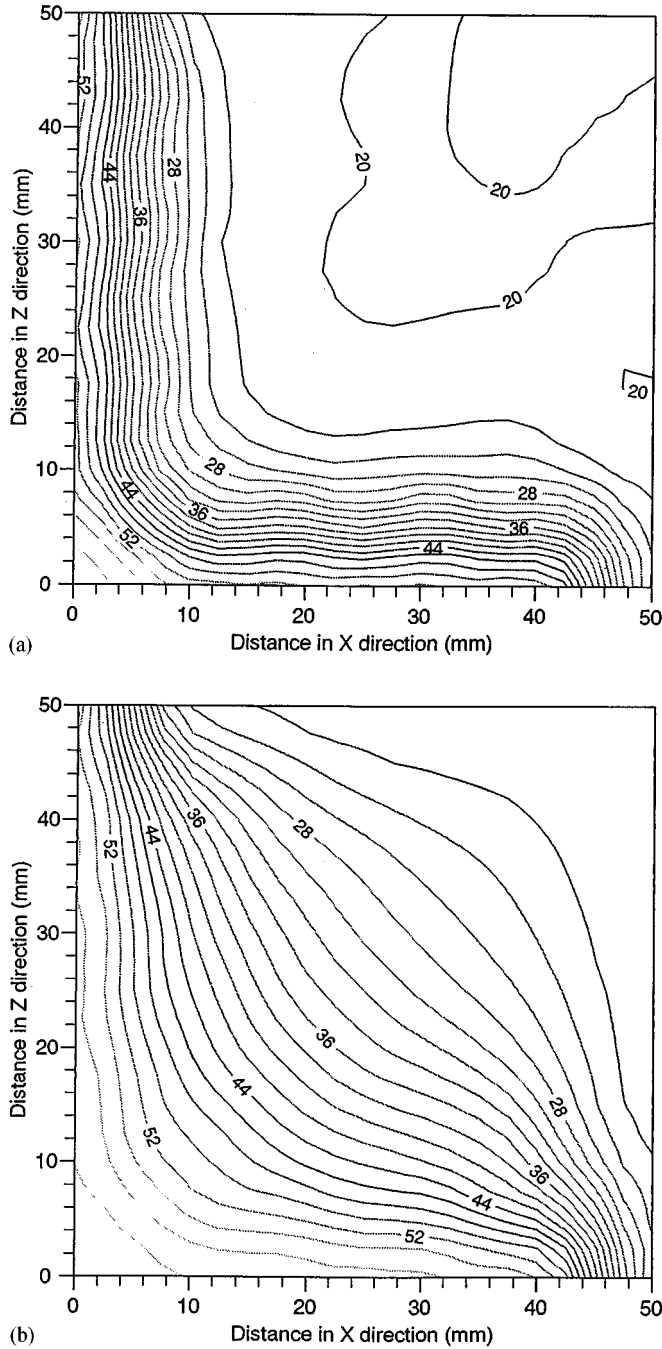


Figure 5(a). Application 1—Thermal distribution for plane Y12.5 at 10 s. (b) Application 1—Thermal distribution for plane Y12.5 at 600 s. (c) Application 1—3D temperature distribution for whole domain. (d) Application 1—A comparison of the equilibrium profile at section X-X between the new model and PAFEC

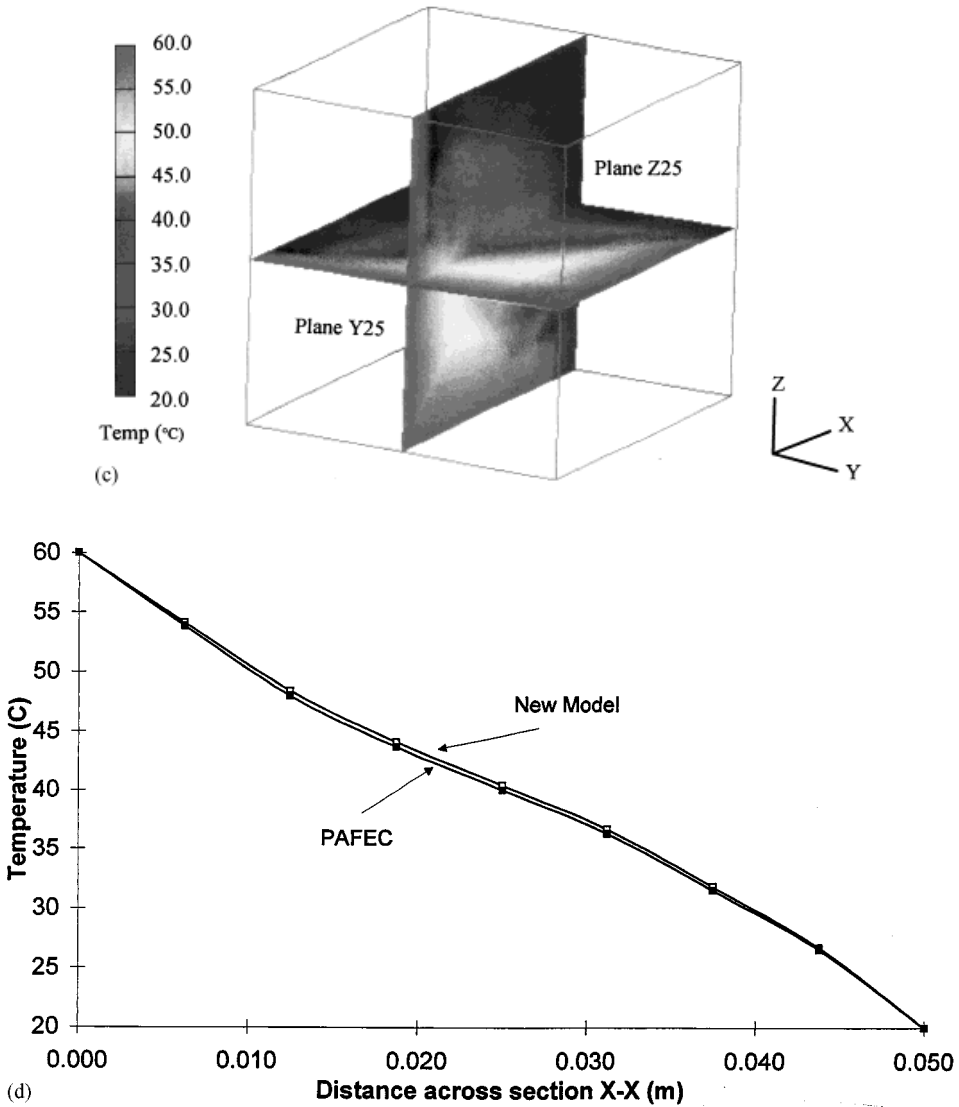


Figure 5 (Continued)

5.3. Application 2—Heat and moisture transfer application

The second application seeks to show effects, through three separate simulations, of gravity, a moisture gradient and a thermal gradient operating in the Z, X and Y dimensions, respectively. The three simulations are run as fully coupled heat and moisture transfer analysis with air pressure assumed to be a constant 100 kPa. Simulation 1 considers the effect alone of a moisture gradient on the domain. Simulation 2 retains the moisture gradient set up in Simulation 1 and

Table I. Soil properties for Leighton Buzzard Sand

| Property/relationship | Value/equation |
|---|--|
| Density (ρ_s) | 2700 kg/m ³ |
| Specific heat capacity (C_{ps}) | 800 J/kgK |
| Intrinsic permeability (k) | 9.6×10^{-11} m ² |
| Porosity (n) | 0.389 |
| Soil water retention curve (Ψ v θ) | $\Psi_r = -2.41 - 0.002\theta_1^{-1.75}$ m $0 \leq \theta_1 \leq 0.2$ $\Psi_r = [\bar{S}(n - \theta_1)]^Q$ m $0.2 \leq \theta_1 \leq n$ where $\bar{S} = 1.101416 \times 10^{-26}$ and $Q = 0.0226249$ |
| Hydraulic conductivity v volumetric liquid content (K_l v θ_l) | $K_l = 1.5 \times 10^{-10} \exp \left[28.061 \frac{\theta_l}{n} - 12.235 \left(\frac{\theta_l}{n} \right)^2 \right]$ m/s |
| Thermal conductivity v volumetric liquid content (λ_c v θ_l) | $\lambda_c = 0.256 + 2.458 [1 - \exp(-22.94\theta_l)]$ W/mK |
| Relative air permeability v volumetric liquid content (k_{ra} v θ_l) | $k_{ra} = (1 - S_e)^2 (1 - S_e^{(2+\varphi)/\varphi})$ m/s where $S_e = \frac{(\theta_l/n) - S_r}{1 - S_r}$ |

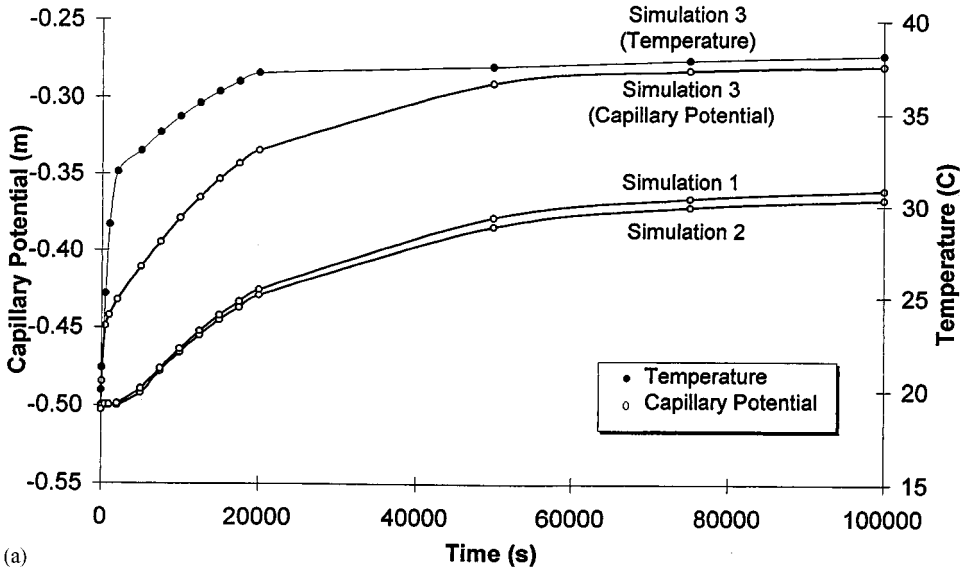
Table II. Summary of boundary conditions used by the simulations in the heat and mass transfer analysis

| Simulation | Gravity | Dirichlet boundary conditions | |
|------------|---------|---|-----------------------------------|
| | | Capillary potential (Ψ) | Temperature (T) |
| 1 | × | − 0.5 m over $X0$ − 0.3 m over $X50$ | — |
| 2 | ✓ | − 0.5 m over $X0$ − 0.3 m over $X50$ | — |
| 3 | ✓ | − 0.5 m over $X0$ − 0.3 m over $X50$ | 20°C over $Y0$ 60°C over $Y50$ |

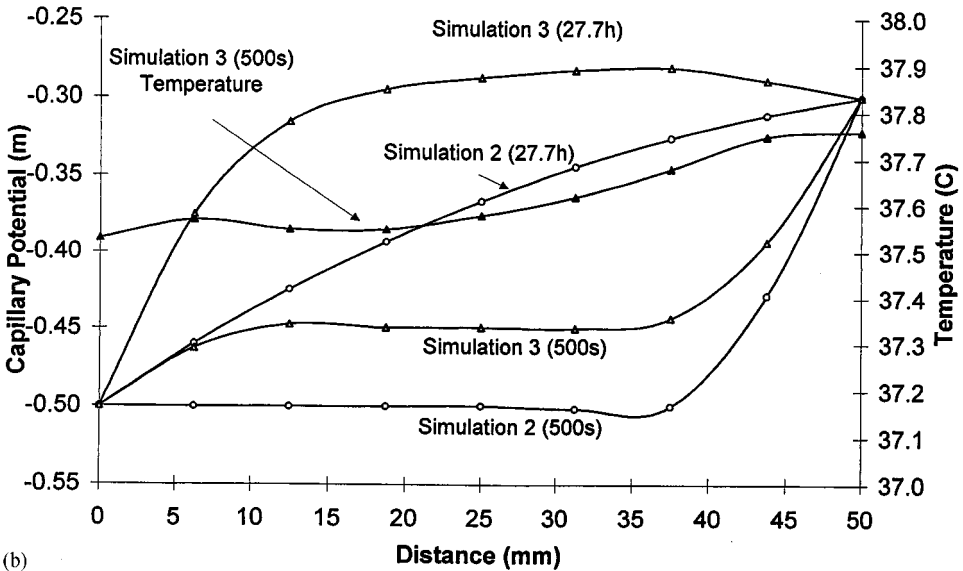
also includes the effects of gravity on the domain. Simulation 3 retains the moisture gradient and gravitational potential and additionally includes a thermal gradient. All simulations are started with uniform initial conditions of − 0.5 m and 20°C for capillary potential and temperature, respectively. All simulations are subjected to Dirichlet capillary potential boundary values of − 0.3 m on face $X50$ and − 0.5 m on face $X0$, inducing a moisture gradient in the X direction. Simulation 2 includes gravitational effects inducing a moisture gradient in the Z (vertical) direction. Simulation 3 is subject to an elevated temperature boundary values of 60°C on face $Y50$ and 20°C on face $Y0$, inducing a thermal gradient in the Y direction. Boundary conditions are summarised in Table II. Unless stated in Table II all other boundaries are non-conducting.

The contribution of each gradient is highlighted as the simulations progress through this analysis. Figures 6(a) to 6(c) present comparisons of the results achieved by each simulation.

Figure 6(a) shows the transient variation of capillary potential (clear markers) and temperature (solid markers) at point 25, 12.5, 25 (X, Z, Y , i.e. a point offset vertically from the centre of the domain) for each simulation. The effect of gravity on the moisture gradient in Simulation 1 can be



(a)



(b)

Figure 6(a). Application 2—Transient variation of temperature and capillary potential at point (25,12.5,25). (b) Application 2—Temperature and capillary potential profiles along section X-X. (c) Application 2—Capillary potential contours after 5000 s on plane Z25

seen by comparison with Simulation 2, which shows the capillary potential variation with time including gravitational potential in the analysis. Initially, gravity seems to cause little effect on the capillary potential distribution but as time increases the influence of gravity on the capillary potential at the sample point becomes more evident as a new gradient is established in the vertical Z dimension.

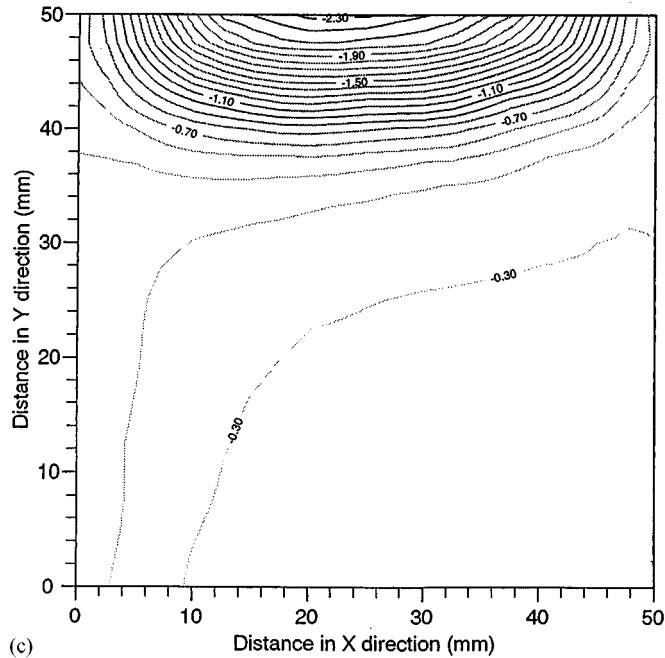


Figure 6 (Continued)

The influence of the addition of a thermal gradient in Simulation 3 is shown by the curve 'Simulation 3' in Figure 6(a). A curve is also provided (represented by solid markers) of the corresponding temperature increase at the point. The elevated temperature has the clear effect of increasing the soil moisture content (i.e. the capillary potential becomes less negative) at this sample point in comparison with the previous moisture content values. The increase is attributed to the hotter temperature at face Y50 driving moisture away thereby increasing the moisture content elsewhere in the cooler regions of the domain. This effect is further highlighted by Figures 6(b) and 6(c).

Figure 6(b) shows section $X-X$ (i.e. Y and Z constant at 25 mm) at two times of 500 and 100,000 s (≈ 27.7 h) for Simulation 2 (moisture and gravity gradients) and Simulation 3 moisture, gravity and thermal gradients). Considering section $X-X$ at 500 s, Simulation 2 yields a constant capillary potential of -0.5 m which is evident to a distance of 32.5 mm. The capillary potential from this point decreases (i.e. becomes less negative) to a value of -0.3 m toward $X = 50$ mm at the boundary signifying infiltration of moisture from this boundary. The section taken at 27.7 h for simulation 2 shows an almost linear variation of capillary potential from the -0.3 m boundary at $X = 50$ mm to the -0.5 m boundary at $X = 0$. The decrease in capillary potential is evident as the infiltration of moisture from $X50$ has progressed across the domain with time.

Simulation 3, which includes the effects of a moisture gradient, gravity and a thermal gradient, shows that the capillary potential has been decreased at a greater rate due to the inclusion of the thermal gradient in the Y dimension at both times. Again this has the effect of increasing the moisture content at this position as moisture is driven away from the Y50 face.

Figure 6(c) shows capillary potential contours at plane cross section Z25 for Simulation 3. At face Y50 large capillary potentials of up to $\Psi = -2.3$ m are experienced due to the drying effect of the elevated temperature. The curved nature of the contours reflects the imposed capillary potential gradient in the X direction. The contour representing -0.5 m penetrates from Y50 to $Y = 36$ mm indicating that moisture has been driven to the cooler areas of the domain.

5.4. Application 3—heat, moisture and air transfer application

This application illustrates the distributions, caused by a simulated heat source, of the three primary variables of ψ , T and P_a . This analysis is run as a fully coupled heat, moisture and air transfer problem. Initial conditions are set as -0.5 m, 20°C and 100 kPa for capillary potential, temperature and air pressure respectively. One element in the domain bordering external faces X0, Z0 and Y0 (shaded in Figure 4(a)) has all nodes fixed at an elevated temperature of 60°C to simulate a heater. All other external boundaries are non-conducting.

Results presented in Figures 7(a) and 7(b). Figure 7(a) shows the transient variation of capillary potential at various points along section A-A (defined in Figure 4(c)). A-A varies in the X dimension at constant values of $Y = 0.0$ mm and $Z = 12.5$ mm. Temperature is also represented on Figure 7(a) as a transient variation at point 25, 12.5, 0.0 (X, Z, Y) and is presented on the figure using solid markers. The capillary potential variation at point (6.25, 12.5, 0.0) starts at the initial value of -0.5 m and then decreases to below -0.46 m at 2500 s. This is caused by moisture being driven from the heater initially increasing the moisture content at this position. From 2500 s the capillary potential then increases to just over -0.485 m at 10 000 s. Considering the temperature at this time is approaching its maximum at this point the moisture content decreases as water is pushed to the further extremes of the cube. This can be seen by the corresponding minimum value of capillary potential of -0.422 m for point (42.75, 12.5, 0.0). From 10,000 s the capillary potential for point (6.25, 12.5, 0.0) then decreases to an equilibrium position at approximately -0.45 m after 75 000 s. As the domain has nearly all reached a maximum temperature of 60°C moisture is no longer driven from the heater and therefore redistributes uniformly around the cube. This is also evident from point (42.75, 12.5, 0.0). The reason that the capillary potential has not returned to its initial value of -0.5 m is due to the fact that air pressure throughout the domain changes uniformly with time.

A qualitative temperature distribution is shown in Figure 7(b) over the whole domain after 100 s. Again red represents 60°C and blue represents 20°C . The external faces of each element are shown in the figure and have been 'shrunk' to allow an internal view of the cube. The progress of the thermal front into the cube is spherical in shape with the origin being at point 0.50, 0 as would be expected.

6. CONCLUSION

A new three-dimensional numerical model of coupled heat, moisture and air transfer in unsaturated soil has been presented for the first time in the literature. The model accommodates the following thermophysical processes:

- (i) moisture transfer in the form of liquid and vapour flow,
- (ii) heat transfer arising from conduction, convection and latent heat of vaporisation, and
- (iii) the bulk flow of dry air and the movement of air in a dissolved state.

A numerical solution of the three-dimensional theoretical formulation was achieved using the finite element method to achieve spatial discretisation and the finite difference method to accommodate the time-varying nature of the problem. In particular, spatial discretization is

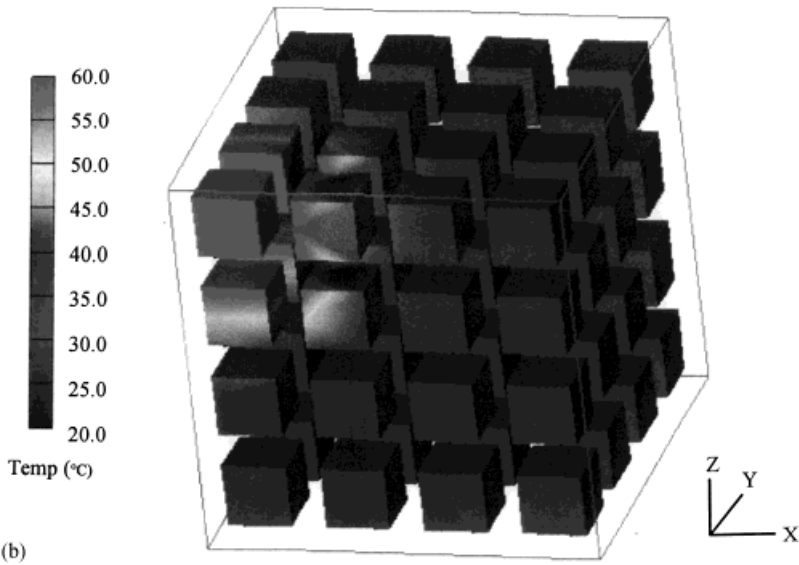
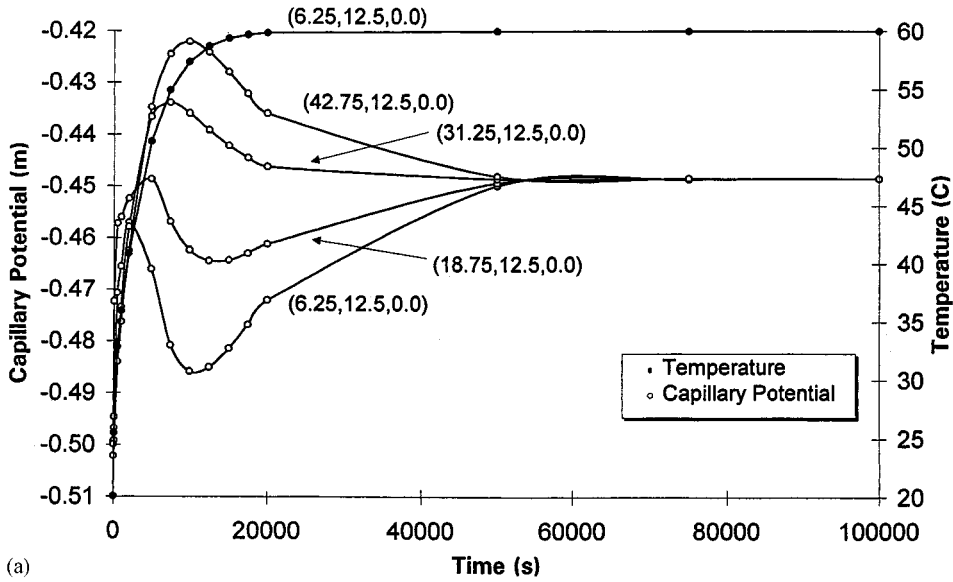


Figure 7. (a) Application 3—Transient variation of capillary potential and temperature at various points along the section A-A (b) Application 3—Temperature variation over the domain after 100 s

achieved using standard 20-node isoparametric brick elements. Numerical integration is achieved using a $3 \times 3 \times 3$ Gaussian method. Time marching is achieved via the use of a fully implicit mid-interval backward difference scheme.

The theoretical basis of the model has been validated against experimental results elsewhere. Therefore attention has been focused in this paper on verification of the new software. This has

been achieved via comparisons with independent solutions of heat, moisture and air transfer in an unsaturated soil. Excellent correlation of results has been achieved thus providing confidence in the new model.

The new model has been applied to a number of test cases which illustrate the need for the development of a model which can fully include three dimensional behaviour. In particular, three applications have been presented each of increasing complexity. The first application illustrates three-dimensional heat transfer. This particular application has been successfully verified against existing commercial finite element software.

In conclusion, a new three-dimensional model for coupled heat, moisture and air transfer has been developed. The model has been verified against independent solutions. A number of applications of the model have illustrated how the coupled processes under consideration may combine to yield complex three-dimensional problems even within a simple geometric domain. Visualization of three-dimensional results has also been addressed.

NOTATION

| | |
|-----------------|--|
| C_{aa} | $[\eta + [H_c - 1]\theta_l]X_{aa}$ |
| C_{aT} | $[\eta + [H_c - 1]\theta]X_{aT} + [H_c - 1]\rho_{da}(\partial\theta_l/\partial T) _\Psi$ |
| $C_{a\Psi}$ | $[\eta + [H_c - 1]\theta_l]X_{aT} + [H_c - 1]\rho_{da}(\partial\theta_l/\partial T) _\Psi$ |
| $C_{L\Psi}$ | $\rho_l(\partial\theta_l/\partial\Psi) _T$ |
| C_{LT} | $\rho_l(\partial\theta_l/\partial T) _\Psi$ |
| C_{pda} | specific heat capacity of dry air |
| C_{pl} | specific heat capacity of soil water |
| C_{ps} | specific heat capacity of soil solids |
| C_{pv} | specific heat capacity of soil vapour |
| $C_{T\Psi}$ | $C_{\rho l}(T - T_r)C_{L\Psi} - C_{\rho da}(\rho_{da}/\rho_l)(T - T_r)C_{L\Psi} + C_{\rho da}(T - T_r)$ $(\eta - \theta_l)X_{a\Psi} + [C_{\rho v}(T - T_r) + L]C_{v\Psi}$ |
| C_{TT} | $H + C_{\rho l}(T - T_r)C_{LT} - C_{\rho da}(\rho_{da}/\rho_l)(T - T_r) + C_{\rho da}(T - T_r)(\eta - \theta_l)X_{aT}$ $+ [C_{\rho v}(T - T_r) + L]C_{vT}$ |
| C_{Ta} | $C_{pda}(T - T_r)(\eta - \theta_l)X_{aa}$ |
| $C_{v\Psi}$ | $[\eta - \theta_l](\rho_0 gh/R_v T) - \rho_0 H(\partial\theta_l/\partial\Psi) _T$ |
| C_{vT} | $- [\eta - \theta_l](\rho_0 \Psi gh/R_v T^2) + [\eta - \theta_l]h\beta - \rho_0 h(\partial\theta_l/\partial T) _\Psi$ |
| $C_{\Psi\Psi}$ | $C_{L\Psi} + C_{v\Psi}$ |
| $C_{\Psi T}$ | $C_{LT} + C_{vT}$ |
| D_{atm} | molecular diffusivity of water vapour in air |
| E | evaporation term (moisture transfer between liquid and vapour phases) |
| $F_{hx(x=1,5)}$ | approximate flux of heat normal to the boundary surface |
| g | acceleration due to gravity |
| H | volumetric heat capacity of unsaturated soil |
| H_c | Henry's constant |
| h | relative humidity |
| K | unsaturated hydraulic conductivity |
| K_a | intrinsic permeability of the air phase |
| K_{aa} | $[\rho_{da}]_{const}(k_a K_{ra}/\mu_a) + (\rho_{da} H_c K/\gamma_w)$ |
| $K_{a\Psi}$ | $[\rho_{da}]_{const} H_c K$ |
| K_{La} | K/g |

| | |
|---------------------------------|---|
| $K_{L\Psi}$ | $\rho_l K$ |
| K_{Ta} | $[C_{pv}\rho_v(T - T_r) + C_{pda}\rho_{da}(T - T_r) + \rho_v L](k_a K_{ra}/\mu_a)$ $+ [C_{pl}K\rho_l(T - T_r)/\gamma_w]$ |
| K_{TT} | $\lambda + C_{pv}\rho_l(T - T_r)K_{v2} + \rho_l L K_{v2}$ |
| $K_{T\Psi}$ | $C_{pl}(T - T_r)K_{L\Psi} + C_{pv}\rho_l(T - T_r)K_{vl} + \rho_l L K_{vl}$ |
| K_{v1} | $- [D_{atm}v\eta\rho_0 gh/\rho_l R_v T]$ |
| K_{v2} | $- D_{atm}v\eta(\nabla T)_a/\rho_l \nabla T [h\beta - \rho_0 \Psi gh/R_v T^2]$ |
| K_{va} | $(\rho_v)_{const}(K_a k_{ra}/\mu_a)$ |
| K_{vT} | $[D_{atm}v\eta(\nabla T)_a/\nabla T][h\beta - (\rho_0 \Psi gh/R_v T^2)]$ |
| $K_{v\Psi}$ | $D_{atm}v\eta\rho_0 gh/R_v T$ |
| $K_{\Psi a}$ | $K_{La} + K_{va}$ |
| $K_{\Psi T}$ | K_{vT} |
| $K_{\Psi\Psi}$ | $K_{L\Psi} + K_{v\Psi}$ |
| k_{ra} | relative permeability of air phase |
| L | latent heat of vapourisation of water |
| N_r, N_s | matrix shape functions associated with element nodal points |
| n | porosity |
| P_a | air pressure |
| P_l | pore liquid pressure |
| R_{da} | specific gas constant for dry air |
| R_v | specific gas constant for water vapour |
| T | absolute temperature |
| T_r | reference temperature |
| $\frac{(\nabla T)_a}{\nabla T}$ | ratio of microscopic temperature gradient in pore space to macroscopic temperature |
| t | time |
| U | liquid velocity |
| V | vapour velocity |
| V_a | air velocity |
| V_{aa} | $- [V_a + H_c U] X_{aa}$ |
| V_{aT} | $- [V_a + H_c U] X_{aT}$ |
| $V_{a\Psi}$ | $- [V_a + H_c U] X_{a\Psi}$ |
| V_l | Volume of soil liquid |
| V_s | Volume of soil solids |
| V_{Ta} | $- C_{pda} V_a(T - T_r) X_{aa}$ |
| V_{TT} | $- \left\{ C_{pl}\rho_l U + C_{pv}\rho_l V + C_{pv}\rho_v V_a + C_{pda}\rho_{da} V_a + C_{pda} V_a(T - T_r) X_{aT} + \right.$ $\left. - \left\{ C_{pv}(T - T_r) V_a[h\beta - (\rho_0 \Psi gh/R_v T^2)] + L V_a[h\beta - (\rho_0 \Psi gh/R_v T^2)] \right\} \right\}$ |
| $V_{T\Psi}$ | $- [C_{pv}(T - T_r) V_a(\rho_0 gh/R_v T) + L V_a(\rho_0 gh/R_v T) + C_{pda}(T - T_r) V_a X_{a\Psi}]$ |
| V_{vT} | $- V_a[h\beta - (\rho_0 \Psi gh/R_v T^2)]$ |
| $V_{v\Psi}$ | $- V_a \rho_0 gh/R_v T$ |
| $V_{\Psi T}$ | V_{vT} |
| $V_{\Psi\Psi}$ | $V_{v\Psi}$ |
| $X_{a\Psi}$ | $\rho_0 gh/R_{da} T$ |
| X_{aT} | $- [P_a/R_{da} T^2 + R_v/R_{da}[h\beta - \rho_0 \Psi gh/R_v T^2]]$ |
| X_{aa} | $1/R_{da} T$ |

| | |
|--------------------|---|
| x, z, y | global co-ordinate system |
| ξ, η, ζ | local co-ordinate system |
| β | $\partial \rho_0 / \partial T$ |
| γ_1 | specific weight of water ($\gamma_1 = \rho_1 g$) |
| θ_1 | volumetric liquid content — $\theta_1 = V_1 / V_s$ |
| λ | thermal conductivity |
| μ | dynamic viscosity of water |
| μ_a | viscosity of the air |
| v | mass flow factor |
| ρ_0 | density of saturated water vapour |
| ρ_1 | density of liquid water |
| ρ_{da} | density of dry air |
| ρ_s | density of soil particles |
| ρ_v | density of water vapour |
| Ψ | capillary potential — $\Psi = (P_1 - P_a) / \gamma_1$ |

REFERENCES

1. H. R. Thomas and M. R. Sansom, (1995) 'Fully coupled analysis of heat, moisture, and air transfer in unsaturated soil.' *ASCE J. Engng. Mech.*, Vol. 121, March, 1995, 392–405.
2. S. D. King 'A potential based model of coupled heat and moisture transfer in unsaturated soil.' *Ph.D. Thesis*. University of Wales, Cardiff, (1991).
3. H. R. Thomas and S. D. King 'Coupled temperature/capillary potential variations in unsaturated soil.' *J. Engng. Mech.*, **117**, 2475–2491 (1991).
4. J. R. Philip and D. A. DeVries, 'Moisture movement in porous materials under temperature gradients.' *Trans. Am. Geophysical Union*, **38**, 222–232 (1957).
5. H. R. Thomas and S. D. King, 'Coupled heat and mass transfer in unsaturated soil—a potential-based solution.' *Int. J. Num. Anal. Meth. Geomech.*, **16**, 757–773 (1992).
6. C. L. W. Li, 'The use of transputers to simulate heat and mass transfer in soils.' *Ph.D. Thesis*. University of Wales, Cardiff, (1992).
7. M. R. Sansom, 'A fully coupled numerical model of moisture, air and heat transfer in unsaturated soil.' *Ph.D. Thesis*. University of Wales, Cardiff, 1995.
8. O. C. Zienkiewicz and R. L. Taylor, (1989) *The Finite Element Method*, McGraw Hill, 4th ed.
9. J. Ewen, 'Combined heat and mass transfer in unsaturated sand surrounding a heated cylinder.' *Ph.D. Thesis*, University of Wales, Cardiff, (1987).
10. N. E. Edlefsen and A. B. C. Anderson, 'Thermodynamics of soil moisture.' *Hilgardia*, **15**(2), 31–298 (1943).
11. L. Barden, 'Consolidation of compacted and unsaturated clays.' *Geotechnique*, London, England **15**(3), 267–286 (1965).
12. E. E. Alonso, F. Batle, A. Gens and A. Lloret, 'Consolidation analysis of partially saturated soils—application to earthdam construction.' *Num. Meth. In Geomech.*, Innsbruck, Austria, 1303–1308 (1988).
13. R. C. Weast, *Handbook of chemistry and physics*, 57th Ed., CRC Press, Cleveland, Ohio (1976).
14. D. W. Pollock, 'Simulation of fluid flow and energy process associated with high-level radioactive waste disposal in unsaturated alluvium.' *Water Resour. Res.*, **22**, 765–775 (1986).
15. O. C. Zienkiewicz and K. Morgan, *Finite elements and approximation*, John Wiley and Sons, New York (1983).
16. B. Irons and S. Ahmad, *Techniques of finite elements*, Ellis Horward Ltd, Chichester, U.K. (1980).
17. J. Ewen and H. R. Thomas, 'The thermal probe—a new method and its use on an unsaturated sand.' *Geotechnique*, London, England, **37**, 91–105 (1987).
18. J. Ewen and H. R. Thomas 'Heating unsaturated medium sand.' *Geotechnique*, London, England, **39**, 455–470 (1989).
19. PAFEC (1984) *Program for Automatic Finite Element Calculations* PAFEC Ltd. Nottingham.
20. A. D. Jefferson, 'Finite element analysis of composite structures' *PhD Thesis*. University of Wales, Cardiff, (1989).
21. H. R. Thomas 'Non-linear analysis of heat and moisture transfer in unsaturated soils.' *J. Engng. Mech.*, **113**, 1163–1180 (1987).